

Evolution of X-ray cavities

Marcus Brüggen^{1*}, Evan Scannapieco² and Sebastian Heinz³

¹*Jacobs University Bremen, P.O. Box 750 561, 28725 Bremen, Germany*

²*School of Earth and Space Exploration, Arizona State University, P.O. Box 871404, Tempe, AZ, 85287-1404, USA*

³*Department of Astronomy, University of Wisconsin, 475 N Charter Street Madison, WI 53706, USA*

Accepted. Received; in original form

ABSTRACT

A wide range of recent observations have shown that AGN-driven cavities may provide the energy source that balances the cooling observed in the centres of “cool core” galaxy clusters. One tool for better understanding the physics of these cavities is their observed morphological evolution, which is dependent on such poorly-understood properties as the turbulent density field and the impact of magnetic fields. Here we combine numerical simulations that include subgrid turbulence and software that produces synthetic X-ray observations to examine the evolution of X-ray cavities in the absence of magnetic fields. Our results reveal an anisotropic size evolution of that is dramatically different from simplified, analytical predictions. These differences highlight some of the key issues that must be accurately quantified when studying AGN-driven cavities, and help to explain why the inferred pV energy in these regions appears to be correlated with their distance from the cluster center. Interpreting X-ray observations will require detailed modeling of effects including mass-entrainment, distortion by drag forces, and projection. Current limitations do not allow a discrimination between purely hydrodynamic and magnetically-dominated models for X-ray cavities.

Key words:

1 INTRODUCTION

Feedback from active galactic nuclei (AGN) is widely believed to be the most promising mechanism to solve a number of problems in our understanding of the history of baryonic structure formation, including: (i) regulating supermassive black hole formation (Churazov et al. 2005; Sijacki & Springel 2006); (ii) setting the upper mass cut-off in the galaxy mass function, and determining its evolution with redshift (Benson et al. 2003; Best et al. 2005); (iii) providing the nongravitational “preheating” that is likely to have been important in determining the entropy profiles of non “cool-core” galaxy clusters (Donahue et al. 2006; Scannapieco & Oh 2004); and (iv) offsetting the radiative losses seen in cool-core galaxy clusters (see e.g., McNamara & Nulsen 2007). Such clusters show strong peaks in their central X-ray surface brightness distributions, indicating that the central gas is cooling rapidly. Yet the deficit of star formation and <1 keV gas (e.g., Rafferty et al. 2006) means that radiative cooling must be balanced by an unknown energy source. Currently, the most successful model for achieving this balance relies on heating from a central AGN; yet the details of this process are poorly under-

stood (e.g., Brüggen & Kaiser 2002; Reynolds et al. 2002; Brighenti & Mathews 2006).

While AGN in cool-core clusters are observed to drive large bubbles into the intracluster medium (ICM) (McNamara et al. 2000; Blanton et al. 2001; Finoguenov & Jones 2001; Nulsen et al. 2005), the synchrotron radiation emitted by the relativistic electrons in these bubbles fades and becomes extremely difficult to detect after about 10^8 years. Moreover, the corresponding X-ray surface brightness depressions are only visible near the centre of the cluster where the contrast is large. AGN have also been observed to induce shocks and/or sonic motions in the ICM that are believed to dissipate their energy into this gas (Fabian et al. 2003; Fabian et al. 2005; Kraft et al. 2007; Ruszkowski et al. 2004; McNamara et al. 2005; Finoguenov et al. 2008; Sanders & Fabian 2008), although the impact of the resulting heating is difficult to quantify observationally. Thus, it is unclear how far AGN-driven cavities rise in the cluster, how they couple to the surrounding medium, and how they evolve.

More specifically, the presence of these cavities has raised a number of key questions. The buoyant bubbles inflated by the central AGN are unstable to the Rayleigh-Taylor (RT) instability, which occurs whenever a fluid is ac-

celerated or supported against gravity by a fluid of lower density. Yet, these cavities appear to be intact even after inferred ages of several 10^8 yrs, as is the case for the outer cavities in Perseus (Nulsen et al. 2005). On the other hand, purely hydrodynamic simulations fail to reproduce these observations. Instead, the RT and other instabilities shred the bubbles in a relatively short time (Brüggen et al. 2005; Heinz et al. 2006; Pizzolato & Soker 2006). Magnetic fields have been shown to alleviate this problem somewhat (Robinson et al. 2004; Jones & De Young 2005; Ruszkowski et al. 2007), but they also reduce the extent to which the interior of the hot bubbles couples to the surrounding medium, making it much more difficult for AGN heating to balance cooling.

In a recent paper, Scannapieco & Brüggen (2008) showed that although pure-hydro simulations indicate that AGN bubbles are disrupted into pockets of underdense gas, more detailed modeling of turbulence indicates that this is a poor approximation to a cascade of structures that continues far below current resolution limits. Using a subgrid turbulence model developed by Dimonte & Tipton (2006), they carried out a series of simulations of AGN heating in a cool-core cluster with the adaptive mesh refinement code, FLASH. These simulations showed that Rayleigh-Taylor instabilities act on subgrid scales to effectively mix the heated AGN bubbles with the ICM, while at the same time preserving them as coherent structures. The AGN bubbles are thus transformed into hot clouds of mixed material as they move outwards in the hydrostatic medium, much as large airbursts lead to a distinctive “mushroom cloud” structure as they rise in the hydrostatic atmosphere of Earth. This allows X-ray cavities to remain intact out to large distances from the cluster centre while still coupling to the surrounding medium.

Alternatively, it has been suggested that instead of underdense pockets of ideal gas, the cavities are produced by magnetically dominated jets (Li et al. 2006). In 3D MHD simulations by Nakamura et al. (2006, 2007) bubbles are inflated by a current-carrying jet that injects magnetic flux into a small volume in the vicinity of the supermassive black hole. The jets are launched by injecting non-force-free poloidal and toroidal magnetic fields, and form large currents which travel along the inner jet axis into the lobes and return on the outer boundary of the lobes, forming a sheath around the jet axis. Like bubbles of hot, underdense gas, such jets expand subsonically into wide lobes that appear cooler than the surrounding medium. Unlike hot, underdense gas, these magnetically dominated bubbles behave differently as they rise through the cluster atmosphere.

Recently, Diehl et al. (2008) investigated whether one can use the measured sizes of X-ray cavities observed at different locations in their host clusters to discriminate between these two models. Compiling the sizes and radial offsets of 64 cavities in the X-ray halos of clusters and groups, they were able to show a tight correlation between these two quantities, which is substantially different than one would expect from simple analytic estimates in the pure-hydro case. From this comparison, they came to the preliminary conclusion that the data favor the current-dominated magneto-hydrodynamic jet model.

While a useful first step, such analytical prescriptions neglect some important physical effects that are likely to

affect the interpretation of the data. While the loss of pressure due to bremsstrahlung radiation is negligible, mass entrainment produced by hydrodynamic instabilities is likely to be important (Pavlovski et al. 2007). This will add to the growth of the bubbles produced by the expansion during the ascent in the stratified atmosphere. In fact, there is some circumstantial evidence for mass entrainment in FR I radio sources. Croston et al. (2008) showed that equipartition internal pressures are typically lower than the external pressures acting on the radio lobes, so that additional non-radiating particles must be present. A correlation between the structure of the radio sources and the apparent pressure imbalance can be taken as observational evidence that entrainment may provide this missing pressure. Moreover, drag forces and acceleration by buoyancy distort the bubbles, complicating the interpretation of bubble radii.

Related to these issues is the question as to how to best measure the energetics of AGN-inflated bubbles. It is now standard procedure to use the size of a bubble and the ambient pressure at its location to get an estimate of the pdV work needed to inflate the bubble, which is then used to infer the energy associated with the outburst (e.g., Birzan et al. 2004). Interestingly, if one plots the inferred energy as a function of radius for the known X-ray cavities, one finds that the energy increases as a function of bubble distance from the cluster centre (Rafferty et al. 2006, see Fig. 8). This effect is not only apparent in a large sample of different clusters, but even within the few individual clusters with known multiple bubbles, such as Hydra A and Perseus. Recently, Sanders & Fabian (2007) reported the possible detection of another cavity in Perseus at very large radii (≈ 170 kpc), and inferred an outburst energy several times higher than that inferred for bubbles at ≈ 30 kpc from the cluster centre. Even larger differences between inner and outer bubbles have been reported in Abell 2204 where the outer bubbles have radii of 240 kpc and 160 kpc (Sanders et al. 2008). Understanding this effect will be crucial in correctly addressing the question whether AGN can be a general solution to the cooling flow problem in clusters and galaxies.

Here we combine adaptive-mesh refinement (AMR) simulations that include a subgrid turbulence model (Scannapieco & Brüggen 2008) with software to produce synthetic X-ray observations to better reproduce the detailed evolution of hydrodynamic bubbles (Heinz & Brüggen 2009). Using these results, we are able to quantify the extent to which hydrodynamic bubbles obey simple analytic relations and the effect of subgrid turbulence. In particular, the inferred sizes of bubbles as a function of the cluster-centric distance in our simulations allow us to directly address the extent to which such observations can be used to constrain the role of magnetic fields in bubble evolution and measure the overall energy input from AGN in the centres of cool-core clusters.

The structure of this work is as follows. In §2 we describe our simulations, spectral modeling, and analysis methods. In §3 we present our results and compare them with analytical estimates and observed trends. Conclusions are given in §4.

2 METHOD

2.1 Code

All simulations were performed with FLASH version 3.0 (Fryxell et al. 2000), a multidimensional adaptive mesh refinement hydrodynamics code, which solves the Riemann problem on a Cartesian grid using a directionally-split Piecewise-Parabolic Method (PPM) solver. While the direct simulation of turbulence is extremely challenging, computationally expensive, and dependent on resolution (e.g., Glimm et al. 2001), its behavior can be approximated to a good degree of accuracy by adopting a subgrid approach.

Recently, Dimonte & Tipton (2006), described a subgrid model that is especially suited to capturing the buoyancy-driven turbulent evolution of AGN bubbles. The model captures the self-similar growth of the RT and Richtmyer-Meshkov (RM) instabilities by augmenting the mean hydrodynamics equations with evolution equations for the turbulent kinetic energy per unit mass and the scale length of the dominant eddies. The equations are based on buoyancy-drag models for RT and RM flows, but constructed with local parameters so that they can be applied to multi-dimensional flows with multiple materials. The model is self-similar, conserves energy, preserves Galilean invariance, and works in the presence of shocks. Although it contains several unknown coefficients, these are determined by comparisons with analytic solutions, numerical simulations, and experiments. In Scannapieco & Brüggén (2008), we describe our implementation of this model into the FLASH code, present several comparisons with analytic results, and discuss its usefulness for properly capturing the physics of AGN-driven cavities in the absence of magnetic fields. The reader is referred to this work. for these and other related discussions.

In the present study, all our simulations are performed in a cubic three-dimensional region 680 kpc on a side, with all reflecting boundaries. For our grid, we chose a block size of 8^3 zones and an unrefined root grid with 8^3 blocks, for a native resolution of 10.6 kpc. The refinement criteria are the standard density and pressure criteria, and we allow for 4 levels of refinement beyond the base grid, corresponding to a minimum cell size of 0.66 kpc, and an effective grid of 1024^3 zones.

2.2 Cluster Profile

For our overall cluster profile, we adopted the model described in Roediger et al. (2007), which was constructed to reproduce the properties of the brightest X-ray cluster A426 (Perseus), which has been studied extensively with CHANDRA and XMM-Newton. In this case, the electron density n_e and temperature T_e profiles are based on the deprojected XMM-Newton data (Churazov et al. 2003) which are also in broad agreement with the CHANDRA data (Schmidt et al. 2002; Sanders et al. 2004). Namely:

$$n_e = \frac{4.6 \times 10^{-2}}{[1 + (\frac{r}{57})^2]^{1.8}} + \frac{4.8 \times 10^{-3}}{[1 + (\frac{r}{200})^2]^{0.87}} \text{ cm}^{-3}, \quad (1)$$

and

$$T_e = 7 \times \frac{[1 + (\frac{r}{71})^3]}{[2.3 + (\frac{r}{71})^3]} \text{ keV}, \quad (2)$$

where r is measured in kpc. Furthermore, the hydrogen number density was assumed to be related to the electron number density as $n_H = n_e/1.2$ according to standard cosmic abundances. The static, spherically-symmetric gravitational potential was set such that the cluster was in hydrostatic equilibrium.

2.3 Bubble generation

X-ray cavities in the ICM are thought to be inflated by a pair of ambipolar jets from an AGN in the central galaxy that inject energy into small regions at their terminal points, which expand until they reach pressure equilibrium with the surrounding ICM (Blandford & Rees 1974). The result is a pair of underdense, hot bubbles on opposite sides of the cluster centre.

In order to produce bubbles, we started the simulation by injecting a total energy of E_{inj} into two small spheres of radius $r_{\text{inj}} = 4.5$ kpc at distances of 13 kpc from the cluster centre. The gas inside these spheres was heated and expanded similar to a Sedov explosion to form a pair of bubbles in a few Myrs, a time much shorter than the rise time of the generated bubbles. The parameters r_{inj} , and E_{inj} were chosen such that these regions reached a radius of $r_{\text{bbl}} = 12$ kpc and a density contrast of approximately $\rho_b/\rho_{\text{amb}} = 0.05$ as compared to the surrounding ICM. However, the dependence of the bubble dynamics on the density contrast, ρ_b/ρ_{amb} , is weak provided that $\rho_b/\rho_{\text{amb}} \ll 1$. For a $\gamma = 5/3$ gas, the energy input during this expansion can be simply calculated as

$$E_{\text{expand}} = \int_{V_{\text{init}}}^{V_{\text{evac}}} dV p = \frac{3p_{\text{evac}} V_{\text{evac}}}{2} \left[\left(\frac{V_{\text{evac}}}{V_{\text{init}}} \right)^{2/3} - 1 \right], \quad (3)$$

where p_{evac} and V_{evac} are the pressure and volume at the evacuated stage at the end of the expansion and V_{init} is the initial volume. Finally, the energy released as the bubble moves outwards to the edge of the cluster is

$$E_{\text{bou}} = \int_{V_{\text{init}}}^{V_{\text{evac}}} dV p = \frac{3p_{\text{evac}} V_{\text{evac}}}{2}. \quad (4)$$

The sum of these two contributions for both bubbles amounted to 1.1×10^{60} ergs.

2.4 Synthetic Chandra observations and spectral modeling

In order to allow a direct comparison of simulation output with X-ray data, we made use of a newly-developed pipeline for post-processing of gridded simulation output. The X-ray-imaging pipeline XIM (see also Heinz & Brüggén 2009) is a publically-available set of scripts that automate the creation of simulated X-ray data for a range of satellites. It takes as input the density, temperature, and velocity, as well as a large number of parameters and provides simulated X-ray data in the form of spectral-imaging data cubes. Simple batch-processing and trivial parallelisation allow the manipulation of these large data cubes, provided that the final output data fit entirely in memory.

XIM is focused on visualizing X-ray data from thermal plasmas. The scripts allow the choice of a user-supplied

spectral model as well as the default thermal APEC plasma emission model (Smith et al. 2001a), which self-consistently calculates the equilibrium ionization balance for a thermal plasma. For a fixed set of abundances and a given temperature, APEC then computes interpolated high resolution model X-ray spectra. Atomic data are taken from the ATOMDB using APED (Smith et al. 2001b) and combined with bremsstrahlung continuum for all species.

Querying APED for every simulated cell is computationally too expensive. For computational convenience and speed, XIM creates a table of model spectra that span a user-supplied energy vector and a logarithmic range of temperatures with a user-supplied minimum and maximum. The spectral contribution of each cell is then logarithmically interpolated from this table. In this paper, we have fixed the relative abundance of all elements heavier than helium at the solar value, but in principle, the metallicity Z of the gas can be specified on a cell-by-cell level, for fixed relative abundances of heavy elements.

2.5 Spectral projection

Having computed the spectral contribution in each cell, XIM then calculated a raw spectral data cube by projecting the data along one of the three Cartesian coordinate axes. Spectra were emission-measure weighted and Doppler shifted with the user-provided radial velocity, neglecting relativistic effects. A user-supplied tracer grid was used to weigh the data by the thermal plasma content of the cell. The spectral grid was oversampled by a factor of three with respect to the final output energy grid to allow accurate representation of Doppler shifts in the output spectra.

The data was further redshifted according to the user-specified cosmological redshift and the coordinate axes are scaled to the proper angular size, given the redshift and cosmological parameters, by default using concordance parameters $\Omega = 1$, $\Omega_\Lambda = 0.7$, $H_0 = 70 \text{ km s}^{-1} \text{ Mpc}^{-1}$. The flux in a cube ($x, y, \text{wavelength}$) was then scaled to the cosmologically correct flux at the given distance. The projected data were processed for foreground photo-electric absorption using the Wisconsin Absorption Model (WABS Morrison & McCammon 1983).

2.6 Virtual observation

Next, the raw spectral-imaging cube ($x, y, \text{wavelength}$) was re-gridded in the two spatial directions onto the detector plate scale of the user-specified instrument. XIM incorporates telescope parameters for CHANDRA, CONSTELLATION-X, XEUS, and XMM-NEWTON and will incorporate a telescope model for IXO once response matrices become available, in our case the Advanced Imaging Spectrometer (ACIS), on board the CHANDRA X-ray observatory. The re-gridded data cube was then convolved with the appropriate spectral response and ancillary response matrices, and the convolution output was re-gridded onto the user-specified energy grid.

The output was convolved with a model point-spread function for the selected telescope. The current version of XIM is limited to a Gaussian point spread function with energy-independent kernel width. It takes into account quantum efficiency and telescope effective area, but

neglects detector non-uniformity, vignetting, and point-spread function variance. The latter effects can in principle be modeled through post-processing with third-party telescope simulators (e.g., MARX) (Wise et al. 1997). Finally, Poisson-distributed photon counts were calculated for a user-specified exposure time.

3 RESULTS AND DISCUSSION

3.1 General Properties

In Fig. 1 - 2 we show synthetic observations for the ACIS-I instrument onboard CHANDRA that covers the band from 0.7-10 keV. ACIS is a powerful tool for conducting imaging, spectroscopic and temporal studies of X-ray sources. The instrument consists of ten Charge Coupled Devices especially designed for efficient X-ray detection and spectroscopy. It is the standard instrument to study X-ray cavities.

We set the cluster to the distance of Perseus ($z = 0.017$) and the observation time to 100 ks, and first considered a case in which the initial bubble radii are $r_{\text{bb1}} = 12 \text{ kpc}$, offset from the cluster centre by 13.5 kpc. Figs. 1 and 2 show two different angles with respect to the axis of the AGN. In Fig. 1 the jet axis, meaning the line connecting the bubble centres, lies in the plane of the sky. In Fig. 2, the jet axis is inclined by 45 degrees with respect to the line of sight.

Synthetic observations from a simulation without sub-grid turbulence corresponding to Fig. 1 and Fig. 2 are shown in Fig. 3 and Fig. 4, respectively. As apparent from the synthetic observations, the differences produced by the subgrid turbulence are significant, especially at times $> 150 \text{ Myrs}$. Without the subgrid model, a bubble does not form a single coherent structure but rather looks patchy, eventually coming apart into resolution-dependent subclumps as described in Scannapieco & Brüggen (2008). The cavities in the run without subgrid turbulence also show a weaker X-ray surface brightness contrast, even though the ambient material gets mixed into the bubble by subgrid turbulence. Current observations of X-ray cavities support the picture from the subgrid simulations, and further observations of bubbles at larger distances from cluster centres will help to probe the stability of the bubbles and check the predictions from these kinds of simulations.

The turbulence also affects the inferred bubble sizes, which have been determined by subtracting a smooth, radially-symmetric background model from the X-ray maps, as is often done with real observations and as shown in the last three panels in Fig. 1 - 4. The corresponding radii are shown in Fig. 5 - 6. In most observed cavities the diameter of all bubbles is larger than the distance of their centres to the AGN, indicating the cavities are relatively young. Hence, in our simulations, we only follow their evolution for a time up to 205 Myrs, and most of the bubbles that have been observed should be compared to the first two panels shown in Fig. 1 -2. At this stage of their evolution, all our bubbles are found to have bright rims. As the bubbles move outwards, they quickly become difficult to detect as the X-ray emissivity is proportional to the square of the density (Enßlin & Heinz 2002).

The decrement in surface brightness of a cavity relative to the surrounding ICM is a strong function of its

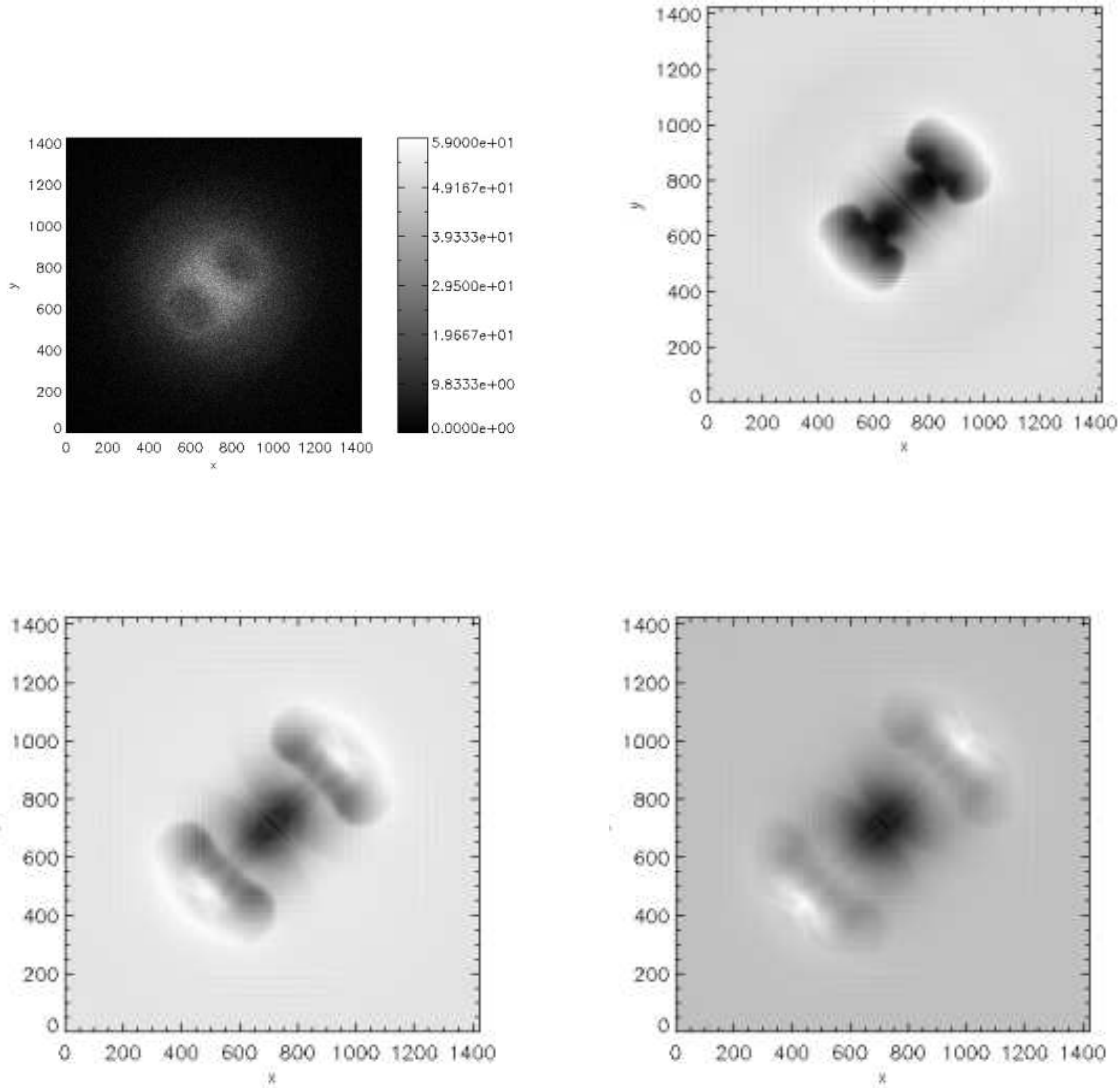


Figure 1. Synthetic CHANDRA observations of a simulated galaxy cluster viewed along an axis perpendicular to the axis of the AGN, at times of 50, 100, 155 and 205 Myrs after the launch of the bubble. The first panel shows the synthetic observation. The units on the x and y -axes are pixels. The greyscale shows the number of counts. The other panels show the X-ray flux with the image of the initial cluster subtracted, which makes it easier to discern the bubbles.

size and distance from the cluster centre. As described in McNamara & Nulsen (2007), a small bubble of radius R on the plane of the sky at a distance r from the cluster centre produces a count deficit which goes as $R^3(1 + r^2/r_c^2)^{-3\beta}$, where r_c is the core radius of the cluster and β a constant. The counts from the ICM scale as $R^2(1 + r^2/r_c^2)^{-3\beta+1/2}$, and the noise in this scales as its square root. Hence, the signal-to-noise ratio scales as $R^2(1 + r^2/r_c^2)^{-3\beta/2-1/4}$, which means that cavities are easiest to detect when they are large and located close to the cluster centre.

3.2 Evolution of bubble size with radius

Diehl et al. (2008) provide simple analytic scaling relations for bubble size as a function of cluster-centric distance, which they used to compare against their compiled observational data set. The first is derived from a simple β -model for the gas pressure of the ICM, given by

$$p_{\text{gas}}(r) = p_0 [1 + (r/r_c)^2]^{-\frac{3\beta}{2}}, \quad (5)$$

where the central pressure, p_0 , is related to the central density, ρ_0 , and isothermal temperature, T , and average molecular weight, \bar{m} , via the equation of state of an ideal gas with an adiabatic index $\Gamma = 5/3$. Assuming that a bubble of initial radius $R_{b,0}$ expands adiabatically in pressure

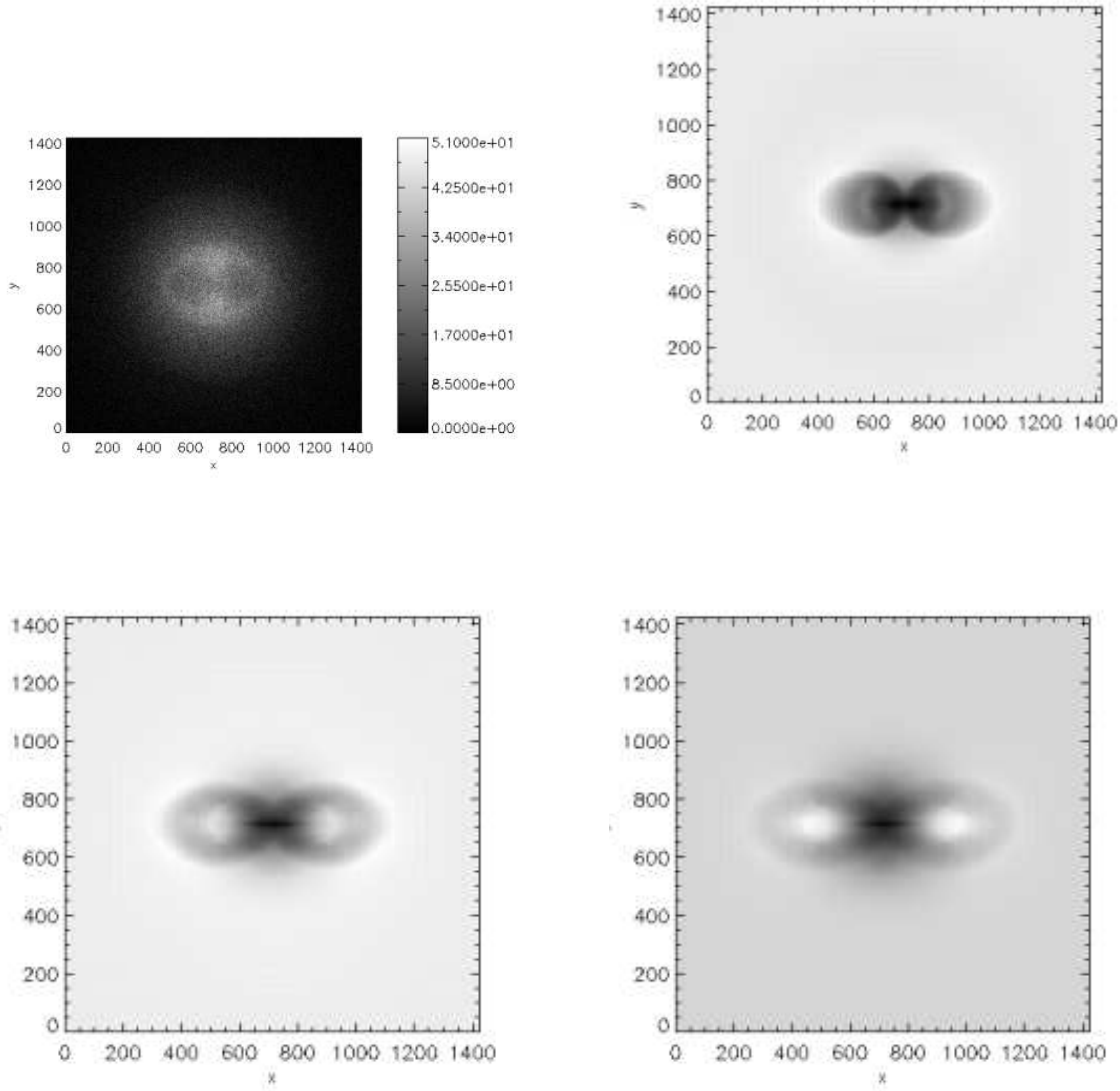


Figure 2. Synthetic CHANDRA observations of a simulated galaxy cluster viewed along an axis that is inclined by 45 deg to jet axis. The panels show the count rates at times of 50, 100, 155 and 205 Myrs after the launch of the bubbles.

equilibrium with the surrounding ICM, its radius R_b should satisfy

$$p_{\text{gas}}(r)R_b^{3\Gamma} = p_{\text{gas}}(r_0)R_{b,0}^{3\Gamma}. \quad (6)$$

Hence, the bubble radius should evolve with distance from the cluster centre, r , as

$$\begin{aligned} R_b(r) &= R_{b,0} [p_{\text{gas}}(r)/p_{\text{gas}}(r_0)]^{-\frac{1}{3\Gamma}} \\ &= R_{b,0} [1 + (r/r_c)^2]^{\frac{\beta}{2\Gamma}}. \end{aligned} \quad (7)$$

Thus, at large radii, the cavities should grow asymptotically as $R_b \propto (r/r_c)^{-\beta/\Gamma}$. For typical values of $\beta = 0.5$ for a cluster and $\Gamma = 5/3$ this gives $R_b \propto (r/r_c)^{3/10}$.

Conversely, for the bubbles produced by current-dominated jets, Diehl et al. (2008) assume a constant cur-

rent along the interior and exterior of the jet axis, such that by Ampère's law $B \propto IR^{-1}$, where I is the current and B is the toroidal magnetic field strength. This means that $p \propto B^2 \propto R^{-2}$, which combined with Eq. (5) means that the bubble size evolves as

$$\begin{aligned} R_b(r) &= R_{b,0} [p_{\text{gas}}(r)/p_{\text{gas}}(r_0)]^{-\frac{1}{2}} \\ &= R_{b,0} [1 + (r/r_c)^2]^{\frac{3\beta}{4}}. \end{aligned} \quad (8)$$

As discussed above, such analytic estimates are not able to capture effects such as mass-entrainment and distortion of the bubbles by drag forces, which are naturally included in the simulation. In fact, our simulations show clearly that the cavities evolve aspherically as they rise through the cluster, expanding quickly in the perpendicular direction, but ex-

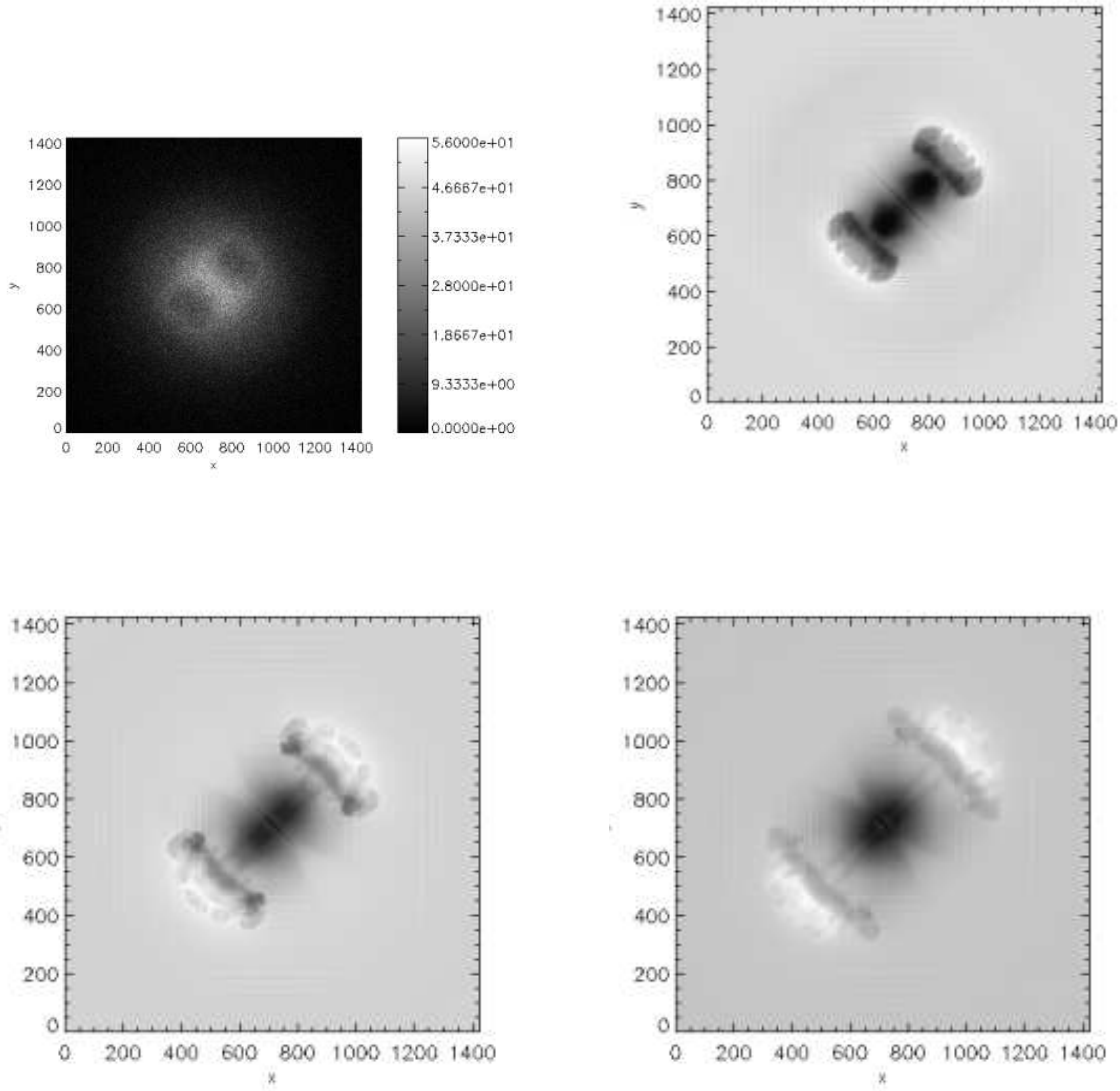


Figure 3. Same as Fig. 1 only without a subgrid model for turbulence.

panding slowly, or even becoming compressed, in the radial direction.

There the radial and perpendicular bubble axes evolve very differently as shown in Figs. 5 and 6. The radial extent of the bubble changes slowly as a function of distance and time, while the perpendicular extent of the bubble changes rapidly. In the case where the AGN axis lies in the plane of the sky, the semimajor axis of the surface brightness depression is oriented perpendicular to the gravitational acceleration, and the bubble appears to flatten as it moves outwards. Conversely, in the case where the AGN axis is tilted by 45 degrees with respect to the line of sight, the projected semimajor axis lies in the projected radial direction, and the bubble appears prolate. In both cases, the major axes grow much more rapidly than the simple analytic prescription given in Eq. (7). On the other hand, after about 150

Myrs, the bubble physically flattens. This becomes visible in the projection shown in Fig. 2. Note also, that in this projection, the bubble never appears to detach from the centre of the image for the time that we have simulated.

One can attempt to constrain bubble properties by confronting the theoretical evolution of the bubble size with the data. However, we do not try this here and it is difficult with the current data. Instead, we merely point out some of the complexities associated with such analyses, even in the non-magnetic case. In Figs. 5 and 6 we have overplotted our measurements from synthetic observations with a sample of bubbles by Rafferty et al. (2006). All the 64 cavities in that sample were observed with CHANDRA. The sample ranges in redshift from $z = 0.0035$ to 0.545 and varies in its composition from groups to rich clusters. For each cavity, a size and position were measured, assum-

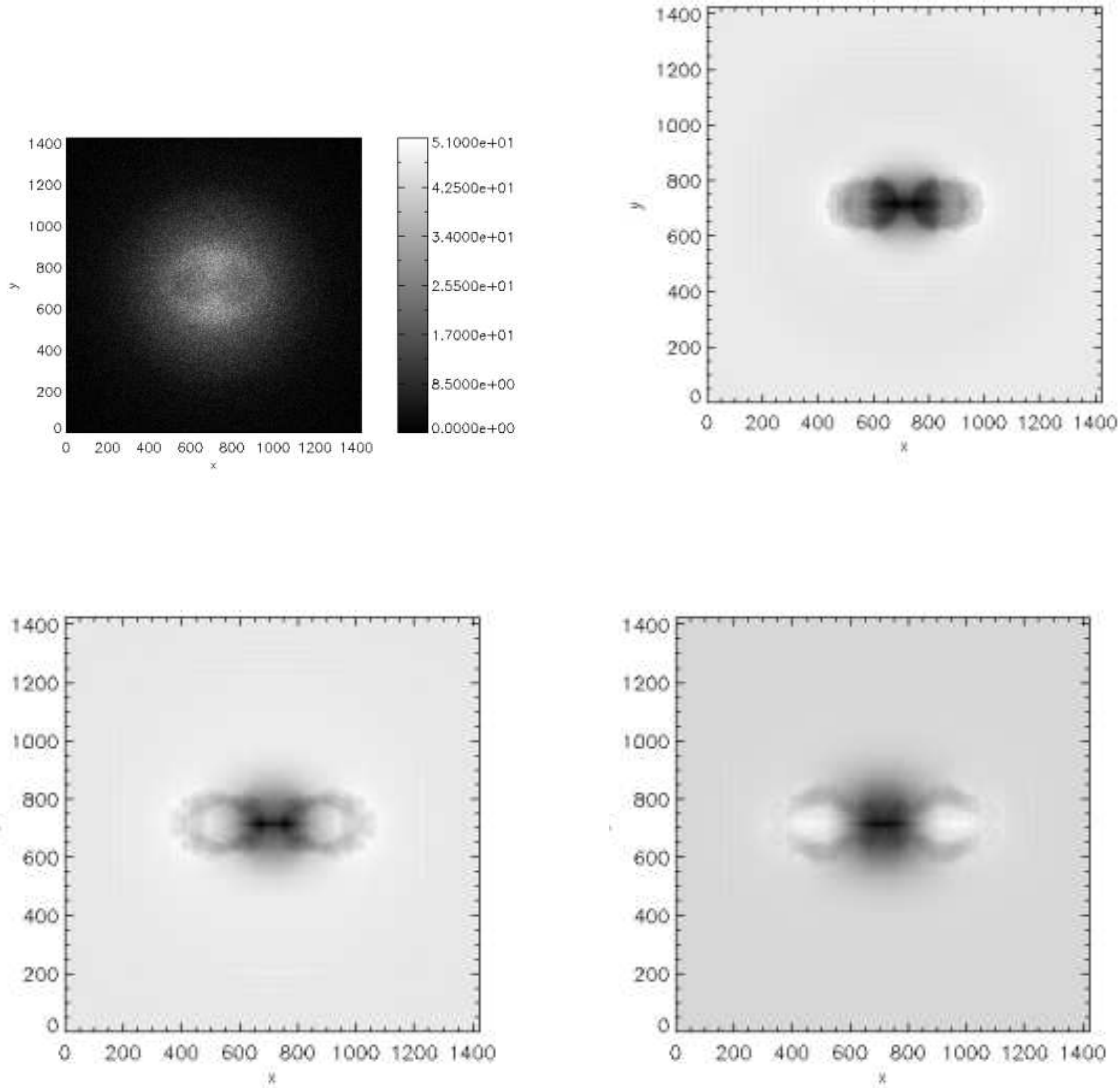


Figure 4. Same as Fig. 2 only without a subgrid model for turbulence.

ing that the cavity extends to the inner edge of any bright surrounding emission. The projected semimajor axis, a , and semiminor axis, b , of the cavities were measured by eye from the exposure-corrected, unsmoothed images.

Diehl et al. (2008) infer that the non-magnetic models are all too shallow to represent the data accurately, while the magnetic models adequately reproduce the steep slope of the correlation. However, when we examine the tangential and radial sizes separately, it is difficult to discard a non-magnetic model. Instead, our simulations show that the evolution of the semimajor and semiminor radii is not in obvious contradiction to the data. In fact, the slopes that we find in Fig. 5 are entirely consistent with the measured bubble sizes. In Fig. 6 we have added analytic estimates according to eqs. (7) & (8), but using the exact pressure profile for the cluster in our simulations ($p \propto nT$, with density and

temperature computed from eqs. 1 & 2). The size-distance relationship of the bubbles is dramatically different from the simple analytical estimate of Eq. (7). Especially the slope of the evolution of the semimajor axis is much steeper than the analytical estimate for the radius as shown by the dashed line.

In our hydrodynamic model of the cavity evolution, the effects of projection are not trivial, and the data points are not just systematically shifted toward smaller radii. The slopes of the size-distance relationship of the bubbles become significantly shallower as the AGN axis tilts toward the line of sight. The appearance of the bubbles show stark differences, especially when the bubbles are further than two bubble radii from the centre of the cluster. Fig. 5 suggest that most observed bubbles come from systems where the AGN axis lies between 90 and 45 degrees from the line of

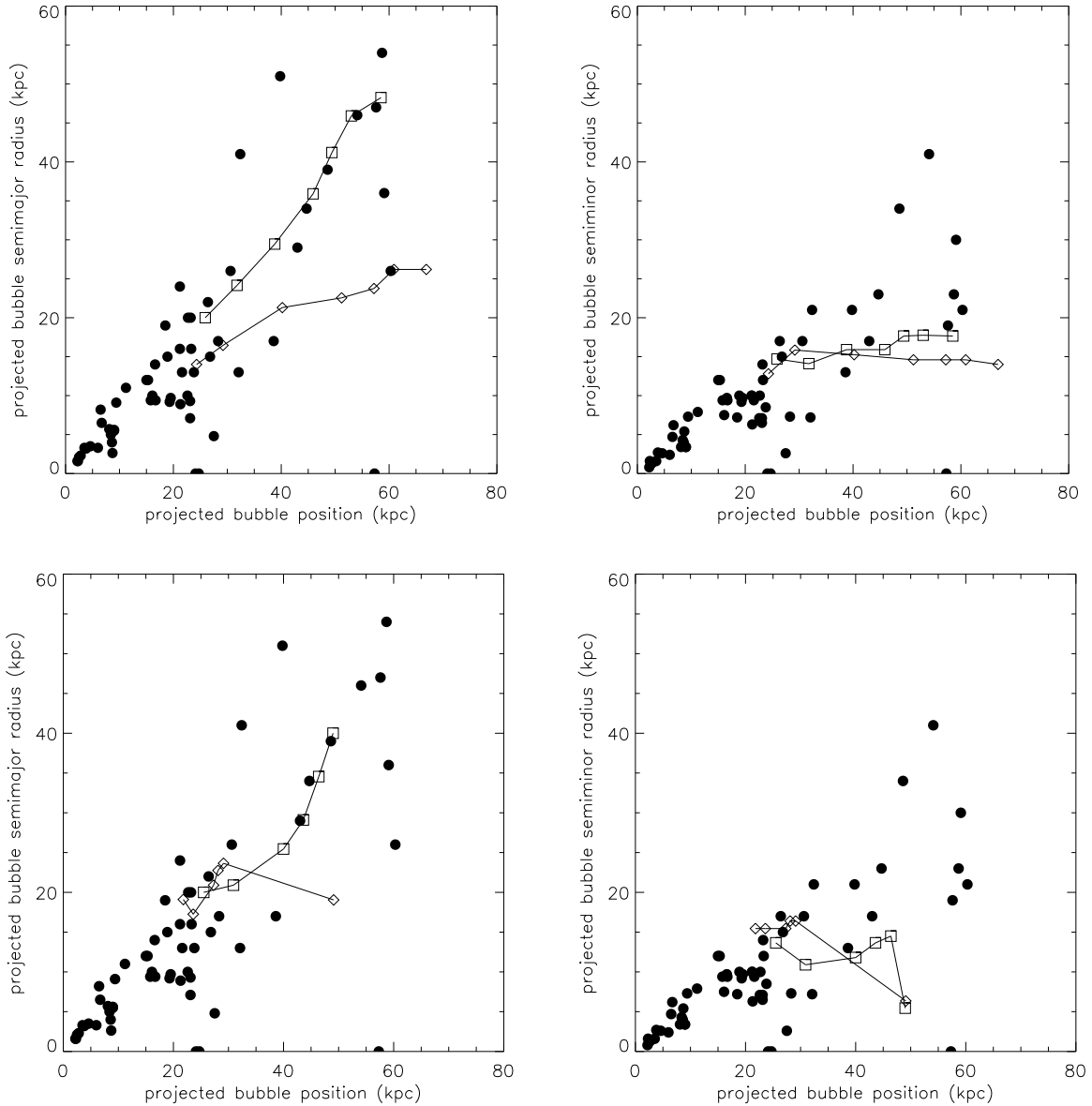


Figure 5. Plot of cavity projected radii versus their projected distance from the cluster centres. The connected squares correspond to the measured radii from synthetic observations where the axis of the AGN lies in the plane of the sky. The diamonds correspond to the case where the AGN axis is inclined by 45 degrees with respect to the line of sight. The unconnected filled circles give the sizes of observed cavities compiled in Rafferty et al. (2006). The bottom row shows the results for a run without a subgrid model. **Left:** semimajor radii, **Right:** semiminor radii.

sight. In fact, this is expected geometrically for a random distribution of bubble axes.

In the case where the AGN axis lies at 45 degrees from the line of sight, the bubbles look more like horseshoes. A confirmation of this will require looking for bubbles at greater distances from the centres in clusters where it is believed that the jet axis is inclined not too far from the line of sight. This could help to verify whether the bubbles are mainly hydrodynamic bubbles. One may speculate that the giant cavities found in Abell 2204 resemble these late-stage horse-shoe shaped bubbles (Sanders et al. 2008).

The spread in bubble radii at a given distance from the centre in Fig. 5 - 6 is due to a spread in the initial

bubble size (or energy) which is determined by properties of the AGN and the host cluster. Diehl et al. (2008) find that the mass of the supermassive black hole and the core radius account for most of the spread. To study the impact of these differences further, we carried out two additional runs, both of which included subgrid turbulence. In one run, we reduced the initial radius of the bubbles to $r_{\text{bbi}} = 6$ kpc, and offset them from the centre by 8.5 kpc, and in a second run we increased the initial radius of the bubbles to $r_{\text{bbi}} = 18$ kpc, offset from the centre by 19.5 kpc. The results of these runs are shown in Fig. 7.

In general, the evolution of the minor and major radii are similar across runs. If the AGN axis lies in the plane

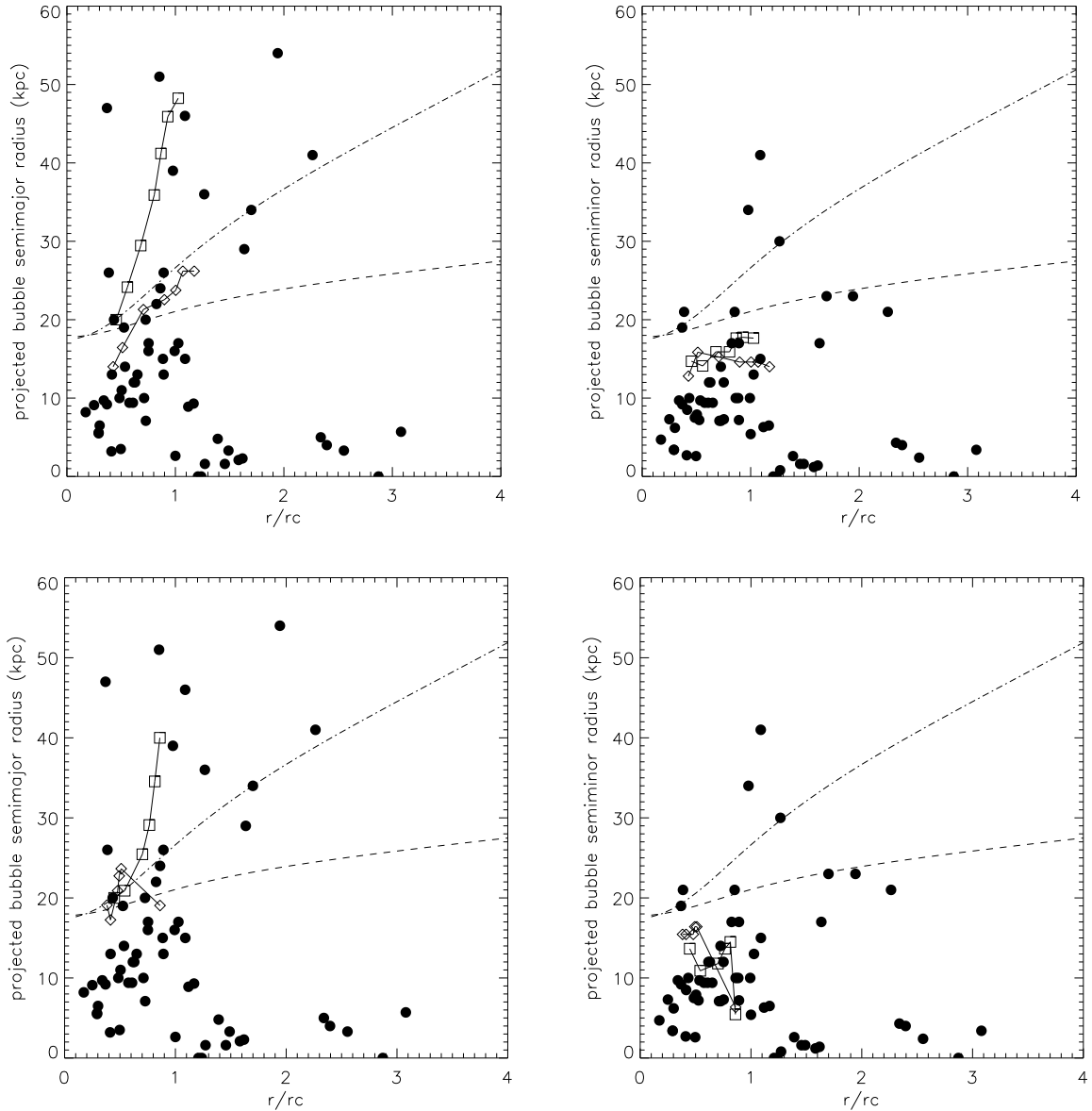


Figure 6. Same as Fig. 5, only the bubble positions are scaled by the core radius of the cluster r_c . The dashed line shows the prediction by Eq. (7) for a fixed value of $R_b(0)$ and $\Gamma = 5/3$, and the dot-dashed line shows the prediction by Eq. (8). The unconnected filled circles give the sizes of observed cavities compiled in Rafferty et al. (2006). **Left:** semimajor radii, **Right:** semiminor radii. The bottom row shows the results for a run without a subgrid model.

of the sky, the major axis, which is perpendicular to the radial direction, evolves much more rapidly than expected from analytic estimates for all choices of initial bubble size. Likewise, in this projection, regardless of initial bubble size, the minor axis grows only very slowly as the cavity moves outward. In all cases, the differences between these runs are well within the observational scatter. In the projection where the AGN axis is inclined by 45 degrees with respect to the line of sight, the major axis, which is now parallel to the radial direction, grows at a moderate rate in all three runs. In all runs this evolution is much more gradual than measured when the bubbles are viewed in the plane of the sky. In all runs, the minor axis of the bubbles remain roughly constant in this projection, even occasionally shrinking slightly. Thus,

initial cavity size and radial offset seem to be relatively minor issues as compared with the anisotropic evolution of the cavities and the angle from which this evolution is viewed.

Finally, Fig. 8 shows the pV energy as function of projected distance from the cluster centre. As discussed above, the pV energy inferred from observations appears to increase with increasing distance, even though this trend is less pronounced at small energies. This may in part be due to the fact that bubbles tend to be overpressured close to their origin, and expand to reach pressure equilibrium as they rise through the ICM. However, excess pressure in the observed cavities is difficult to measure, except indirectly through the presence of shocks and sound waves.

A second possibility for the radial increase in inferred

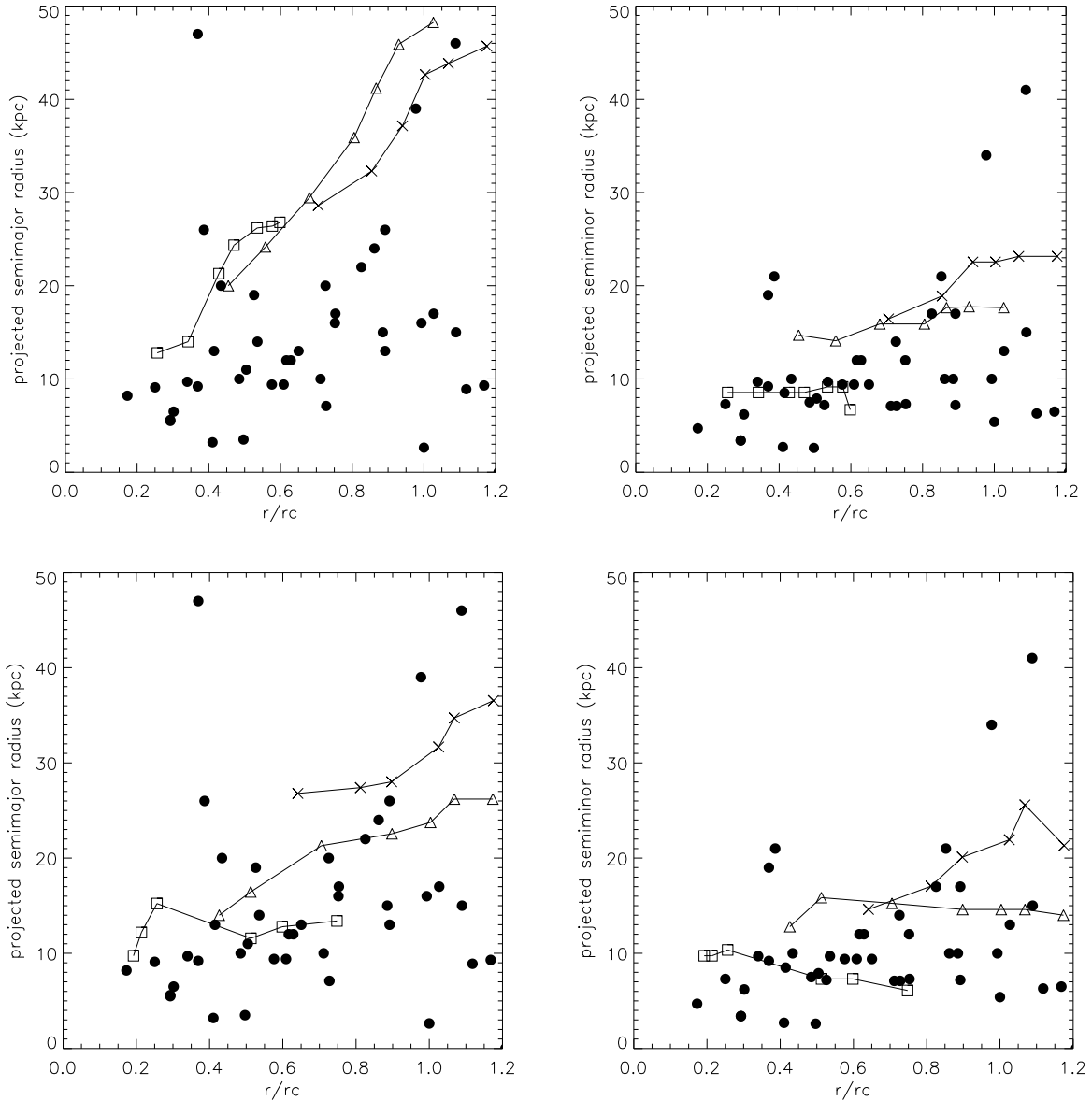


Figure 7. Semimajor (left) and semiminor (right) projected radii versus bubble positions scaled by the core radius of the cluster r_c . The lines correspond to runs with three different sizes for the initial bubbles. Squares: small bubbles (6 kpc), triangles: medium-sized bubbles (12 kpc), crosses: large bubbles (18 kpc). The unconnected filled circles give the sizes of observed cavities compiled in Rafferty et al. (2006). The top row corresponds to the case where the axis of the AGN lies in the plane of the sky; the bottom row displays results for the case where the AGN axis is inclined by 45 degrees with respect to the line of sight.

pV is the entrainment of ambient material. In fact, this is the main reason for the increase in our simulations, as in our model the bubbles quickly reach pressure equilibrium with the surrounding medium, well before moving noticeably out from the cluster centre. Over the 200 Myrs that we simulate, we find that the inferred pV energy for the same bubble grows by a factor of 2 in the case where the AGN axis lies in the plane of the sky. In the case where the AGN axis is inclined by 45 degrees with respect to the line of sight, the inferred pV energy grows hardly at all. In the latter case, the greater apparent pressures (because the bubbles are further in) are offset by the bubbles appearing to be smaller.

The measured energies are more reliable when the bub-

bles are further from the centre of the cluster, which unfortunately, is where they are most difficult to observe. Overall, the error introduced into estimates of the pV energy by these effects is of the same magnitude as the error related to the unknown equation of state of the plasma inside the bubbles.

4 CONCLUSIONS

The nature of AGN-driven X-ray cavities remains one of the major outstanding questions in understanding the physics of cool-core galaxy clusters. While the observed morphologies and sizes of the cavities provide us with useful clues as to

the processes at work in these regions, interpretation of the observations is far from straightforward.

In this study we have focused on a model in which X-ray cavities evolve purely hydrodynamically, and reconstructed their detailed evolution using of two major tools: AMR simulations that include subgrid turbulence and synthetic X-ray software that produces realistic observations from these simulations. Together these tools allow us to capture such important effects as mass-entrainment, distortion of the bubbles by drag forces, and observational effects. These effects lead to an evolution that is drastically different than expected from simple analytic estimates.

In particular, we find that while the radial extent of the cavities changes slowly as a function of distance and time, they expand rapidly in the perpendicular direction. The result is a complex evolution that is highly dependent on viewing angle and difficult to compare conclusively with observations. Although analytic estimates of non-magnetic models evolve too slowly to match the observations, our simulations show that the evolution of the semimajor and semiminor radii is not in obvious contradiction to the data. In fact, our simulations naturally reproduce the overall trend for inferred pV energies of observed X-ray cavities to increase as a function of distance from the cluster centre, an effect that is largely due to mixing of entrained material into the rising cavities. The size evolution we find is in general good agreement with the measured bubble sizes, although there is a large spread in observational data, and a strong dependence on the direction from which the cavities are viewed. Indeed, the flattening and projection of X-ray cavities have much stronger effects on our results than initial bubble size and radius.

Finally, some words of caution. Our simulations start from a very simplified setup. In reality, the bubbles are inflated by jets continuously over some time. Also the host system will be dynamic, leading to a more complex evolution than the simulations presented here can capture. One example are the bubbles in Hydra that do not look like the bubbles we have shown here. In the Hydra cluster, a rapid succession of outbursts from the AGN have continued to fuel the bubbles to produce a partially interconnected series of bubbles that still have some momentum imparted by the original jet. More realistic simulations of specific systems that are designed to reproduce all observed features are needed in order to make better inferences on the nature of X-ray cavities. This, in combination with low-frequency radio observations, will help to understand these elusive and crucial features of cosmic structure.

ACKNOWLEDGEMENTS

MB acknowledges the support by the DFG grant BR 2026/3 within the Priority Programme ‘‘Witnesses of Cosmic History’’ and the supercomputing grants NIC 2195 and 2256 at the John-Neumann Institut at the Forschungszentrum Jülich. All simulations were conducted on the Saguaro cluster operated by the Fulton School of Engineering at Arizona State University. The results presented were produced using the FLASH code, a product of the DOE ASC/Alliances-funded Center for Astrophysical Thermonuclear Flashes at the University of Chicago.

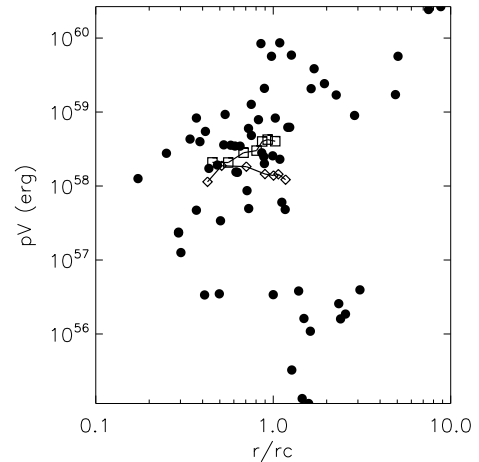


Figure 8. pV energy as function of projected distance from the cluster centre. Again squares correspond to synthetic observations where the axis of the AGN lies in the plane of the sky; diamonds correspond to the case where the AGN axis is inclined by 45 degrees with respect to the line of sight. The unconnected filled circles give the sizes of observed cavities compiled in Rafferty et al. (2006).

REFERENCES

- Birzan L., Rafferty D. A., McNamara B. R., Wise M. W., Nulsen P. E. J., 2004, *ApJ*, 607, 800
 Benson A. J., Bower R. G., Frenk C. S., Lacey C. G., Baugh C. M., Cole S., 2003, *ApJ*, 599, 38
 Best P. N., Kauffmann G., Heckman T. M., Brinchmann J., Charlot S., Ivezić Ž., White S. D. M., 2005, *MNRAS*, 362, 25
 Blandford R. D., Rees M. J., 1974, *MNRAS*, 169, 395
 Blanton E. L., Sarazin C. L., McNamara B. R., Wise M. W., 2001, *ApJ*, 558, L15
 Brighenti F., Mathews W. G., 2006, *ApJ*, 643, 120
 Brüggen M., Kaiser C. R., 2002, *Nature*, 418, 301
 Brüggen M., Ruszkowski M., Hallman E., 2005, *ApJ*, 630, 740
 Churazov E., Forman W., Jones C., Böhringer H., 2003, *ApJ*, 590, 225
 Churazov E., Sazonov S., Sunyaev R., Forman W., Jones C., Böhringer H., 2005, *MNRAS*, 363, L91
 Croston J. H., Hardcastle M. J., Birkinshaw M., Worrall D. M., Laing R. A., 2008, *MNRAS*, 386, 1709
 Diehl S., Li H., Fryer C. L., Rafferty D., 2008, *ApJ*, 687, 173
 Dimonte G., Tipton R., 2006, *Physics of Fluids*, 18, 085101
 Donahue M., Horner D. J., Cavagnolo K. W., Voit G. M., 2006, *ApJ*, 643, 730
 Enßlin T. A., Heinz S., 2002, *A&A*, 384, L27
 Fabian A. C., Reynolds C. S., Taylor G. B., Dunn R. J. H., 2005, *MNRAS*, 363, 891
 Fabian A. C., Sanders J. S., Allen S. W., Crawford C. S., Iwasawa K., Johnstone R. M., Schmidt R. W., Taylor G. B., 2003, *MNRAS*, 344, L43
 Finoguenov A., Jones C., 2001, *ApJ*, 547, L107
 Finoguenov A., Ruszkowski M., Jones C., Brüggen M., Vikhlinin A., Mandel E., 2008, *ApJ*, 686, 911

Fryxell B., Olson K., Ricker P., Timmes F. X., Zingale M., Lamb D. Q., MacNeice P., Rosner R., Truran J. W., Tufo H., 2000, *ApJS*, 131, 273

Glimm J., Grove J. W., Li X. L., Oh W., Sharp D. H., 2001, *J. Comput. Phys.*, 169, 652

Heinz S., Brüggem M., 2009, *ApJ* submitted

Heinz S., Brüggem M., Young A., Levesque E., 2006, *MNRAS*, 373, L65

Jones T. W., De Young D. S., 2005, *ApJ*, 624, 586

Kraft R. P., Nulsen P. E. J., Birkinshaw M., Worrall D. M., Penna R. F., Forman W. R., Hardcastle M. J., Jones C., Murray S. S., 2007, *ApJ*, 665, 1129

Li H., Lapenta G., Finn J. M., Li S., Colgate S. A., 2006, *ApJ*, 643, 92

McNamara B. R., Nulsen P. E. J., 2007, *ARA&A*, 45, 117

McNamara B. R., Nulsen P. E. J., Wise M. W., Rafferty D. A., Carilli C., Sarazin C. L., Blanton E. L., 2005, *Nature*, 433, 45

McNamara B. R., Wise M., Nulsen P. E. J., David L. P., Sarazin C. L., Bautz M., Markevitch M., Vikhlinin A., Forman W. R., Jones C., Harris D. E., 2000, *ApJ*, 534, L135

Morrison R., McCammon D., 1983, *ApJ*, 270, 119

Nakamura M., Li H., Li S., 2006, *ApJ*, 652, 1059

Nakamura M., Li H., Li S., 2007, *ApJ*, 656, 721

Nulsen P. E. J., Hambrick D. C., McNamara B. R., Rafferty D., Birzan L., Wise M. W., David L. P., 2005, *ApJ*, 625, L9

Pavlovski G., Kaiser C. R., Pope E. C. D., 2007, *ArXiv e-prints*

Pizzolato F., Soker N., 2006, *MNRAS*, 371, 1835

Rafferty D. A., McNamara B. R., Nulsen P. E. J., Wise M. W., 2006, *ApJ*, 652, 216

Reynolds C. S., Heinz S., Begelman M. C., 2002, *MNRAS*, 332, 271

Robinson K., Dursi L. J., Ricker P. M., Rosner R., Calder A. C., Zingale M., Truran J. W., Linde T., Caceres A., Fryxell B., Olson K., Riley K., Siegel A., Vladimirova N., 2004, *ApJ*, 601, 621

Roediger E., Brüggem M., Rebusco P., Böhringer H., Churazov E., 2007, *MNRAS*, 375, 15

Ruszkowski M., Brüggem M., Begelman M. C., 2004, *ApJ*, 611, 158

Ruszkowski M., Enßlin T. A., Brüggem M., Heinz S., Pfrommer C., 2007, *MNRAS*, 378, 662

Sanders J. S., Fabian A. C., 2007, *MNRAS*, 381, 1381

Sanders J. S., Fabian A. C., 2008, *MNRAS*, 390, L93

Sanders J. S., Fabian A. C., Allen S. W., Schmidt R. W., 2004, *MNRAS*, 349, 952

Sanders J. S., Fabian A. C., Taylor G. B., 2008, *ArXiv e-prints*

Scannapieco E., Brüggem M., 2008, *ApJ*, 686, 927

Scannapieco E., Oh S. P., 2004, *ApJ*, 608, 62

Schmidt R. W., Fabian A. C., Sanders J. S., 2002, *MNRAS*, 337, 71

Sijacki D., Springel V., 2006, *MNRAS*, 366, 397

Smith R. K., Brickhouse N. S., Liedahl D. A., Raymond J. C., 2001a, *ApJ*, 556, L91

Smith R. K., Brickhouse N. S., Liedahl D. A., Raymond J. C., 2001b, in Ferland G., Savin D. W., eds, *Spectroscopic Challenges of Photoionized Plasmas Vol. 247 of Astronomical Society of the Pacific Conference Series*, Stan-

dard Formats for Atomic Data: the APED. pp 161–+

Wise M. W., Huenemoerder D. P., Davis J. E., 1997, in Hunt G., Payne H., eds, *Astronomical Data Analysis Software and Systems VI Vol. 125 of Astronomical Society of the Pacific Conference Series*, Simulated {AXAF} Observations with {MARX}. pp 477–+

This paper has been typeset from a $\text{\TeX}/\text{\LaTeX}$ file prepared by the author.